

Investigation on particle assisted through-mask electrochemical etching of micro pits array

Liqun Du (✉ duliquun@dlut.edu.cn)

Mingxin Yu

Ke Zhai

Kunming Zheng

Haohao Cheng

Shuxuan Wang

Junshan Liu

Research Article

Keywords: particle, through-mask electrochemical etching, localization, uniformity

Posted Date: August 1st, 2022

DOI: <https://doi.org/10.21203/rs.3.rs-1891938/v1>

License:  This work is licensed under a Creative Commons Attribution 4.0 International License.

[Read Full License](#)

Investigation on particle assisted through-mask electrochemical etching of micro pits array

Liqun Du^{a, b, *}, Mingxin Yu^a, Ke Zhai^c, Kunming Zheng^a, Haohao Cheng^a, Shuxuan Wang^a,
Junshan Liu^{a, b, *}

^a Key Laboratory for Micro/Nano Technology and System of Liaoning Province, Dalian University of Technology, Dalian 116024, China;

^b Key Laboratory for Precision and Non-traditional Machining Technology of Ministry of Education, Dalian University of Technology, Dalian 116024, China;

^c National & Local Joint Engineering Research Center of Metrology Instrument and System, College of Quality and Technical Supervision, Hebei University, Baoding, 071002, China;

* Corresponding Author

E-mail: duliquan@dlut.edu.cn; liujs@dlut.edu.cn

Abstract

Microstructures are applied in various fields to improve the friction and lubrication of mechanical components. Through-mask electrochemical etching (TMEE) has shown good feasibility in machining microstructures array. However, the machining precision of microstructures gradually decreases with increasing etching depth in TMEE. Localization and uniformity are essential indicators of machining precision in TMEE. Herein, particle assisted through-mask electrochemical etching (PA-TMEE) method was proposed to improve the localization and uniformity. Firstly, a coupled multi-physical field model, including gas-liquid two-phase flow, particle motion, and electrochemical processes, was established and adopted to predict the profiles of micro pits. Secondly, a comparison experiment between PA-TMEE and traditional TMEE was performed. The experimental results show that using PA-TMEE instead of TMEE resulted in improved localization and uniformity of the micro pits array. Then, the paper analyzed the effect of particle diameter and content on micro pits. When the particle diameter was 40 μm , and the particle content was 6 g/L, the maximum etching factor was 2.4. The minimum coefficient of variation of the diameter and depth of micro pits were 3.3% and 5.2%. Finally, The machining mechanism of PA-TMEE was analyzed by Scanning Electron Microscopy and Energy Dispersive Spectrometer.

Keywords: particle; through-mask electrochemical etching; localization; uniformity

1 Introduction

Microstructures have been frequently exploited to improve component tribological qualities [1-4]. A number of methods have been developed to produce microstructures in different ways, such as laser beam machining [5], micro-milling [6], electrical discharge machining [7], and through-mask electrochemical etching (TMEE) [8, 9]. Compared to these methods, TMEE is a promising method for microstructures preparation with no tool wear, no heat-affected layers, and high machining efficiency.

As a result of anodic passivation, TMEE is relatively low precision and is mainly used for machining shallow textures [10, 11]. In order to improve the machining precision of TMEE, localization and uniformity are widely concerned and used to evaluate the machining precision of TMEE. The etching factor (EF) is used to describe the etching localization. The ratio of the standard deviation of the micro pits to the mean value is defined as the coefficient of variation (CV). CV_{diameter} and CV_{depth} describe the uniformity of the diameter and depth of micro pits. Notably, a smaller CV indicates better uniformity. Many have developed TMEE machining to improve localization and uniformity. Qian [12] proposed the auxiliary anode to improve localization. The auxiliary anode reduced the current density around the etching area. The diameter of the micro dimples was reduced from 400 μm to 270 μm , and the etching depth was reduced from 18 μm to 17 μm . The addition of the auxiliary anode increased the EF from 0.18 to 0.49. Chen [13] prepared uniform micro-dimple arrays with a diameter of 143 μm and a depth of 35 μm using an auxiliary anode. The normalized diameter of the micro-dimple arrays increased from 0.8 to 0.95, and the normalized depth increased from 0.6 to 0.95 (EF was 1.6). Zhang [14] developed sandwich-like TMEE to improve uniformity by uniformizing the current distribution of the anode. When the etching diameter was 109 μm , and the etching depth was 11.2 μm , the EF was 2.5. The diameter and depth standard deviations were 0.731 μm and 1.241

μm , respectively (CV_{diameter} was 0.7% and CV_{depth} was 11.1%). In addition, to effectively remove bubbles and insoluble electrolysis products, porous cathodes were introduced into sandwich-like TMEE. The average diameter of etching micro dimples was 111 μm , and the average depth of etching micro dimples was 9.2 μm . The diameter and depth standard deviations were 2.39 μm and 1.51 μm , respectively [15] (EF was 1.7; CV_{diameter} was 2.2%, and CV_{depth} was 16.4%). Pan [16] proposed a high-pressure hydrostatic electrolyte to improve the uniformity of TMEE. Micro dimple arrays were prepared with an average etching diameter of 105.95 μm and an etching depth of 9.79 μm . Corresponding the standard deviations of 0.59 μm and 0.21 μm (EF was 3.3; CV_{diameter} was 0.6%, and CV_{depth} was 2.1%). Based on the above literature, the maximum etching depth does not exceed 35 μm . The localization and uniformity of deep metal microstructures in TMEE are rarely studied.

Deep metal microstructures are widely used in various research fields such as aerospace, optical instrumentation, automotive and biomedical technology. Deep metal microstructures have been increasing interest [17-19]. However, the poor localization and uniformity of the deep metal microstructures array limit the application of TMEE. TMEE involves several physical and chemical processes such as electric field distribution, gas transfer, electrolyte flow, and electrochemical reactions. Significantly, the passivation film prevents the mass transfer and electrochemical reactions at the interface. This phenomenon intensifies with increasing etching depth. Therefore, it is extremely challenging to improve the localization and uniformity of deep metal microstructures [20, 21].

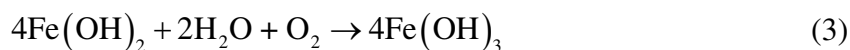
This study introduced particles in TMEE to improve localization and uniformity. Firstly, a PA-TMEE simulation model was established to analyze the influence of particle erosion on the diameter and depth of the micro pits array. Secondly, comparative experiments demonstrated that introducing particles can improve the localization and uniformity of the micro pits array. Then, the effect of the

particle diameter and content on the localization and uniformity of the micro pits array was investigated. Finally, the machining mechanism of PA-TMEE was investigated by Scanning Electron Microscopy (SEM) and Energy Dispersive Spectrometer (EDS).

2 Working principle and simulation analysis

2.1 Working principle of the PA-TMEE method

The anode surface is oxidized during the PA-TMEE, as shown in equations (1)–(3). Passivation film (insoluble electrochemical products) seriously affects electrochemical etching. It is worth noting that, on the one hand, passivation film can reduce lateral erosion. On the other hand, the excessive passivation film can prevent or terminate the TMEE. The SiC particles are driven within the electrolyte and erode the bottom of the micro pits. Therefore, the passivation film is selectively removed from the bottom of the micro pits. Then, the metal surface without the passivation film continues to dissolve, resulting in a deep etching. The schematic diagram of the principle of PA-TMEE to improve the localization is shown in Fig. 1(a). For large-area micro pits array, the etching at the edge of the workpiece is usually more significant than that at the center due to the edge effect of the electric field [13, 22]. The difference in etching amount causes a non-uniform distribution of the passivation film content. In other words, the passivation film content varied with the position. However, particle erosion can significantly reduce the non-uniformity of the passivation film distribution, as shown in Fig. 1(b).



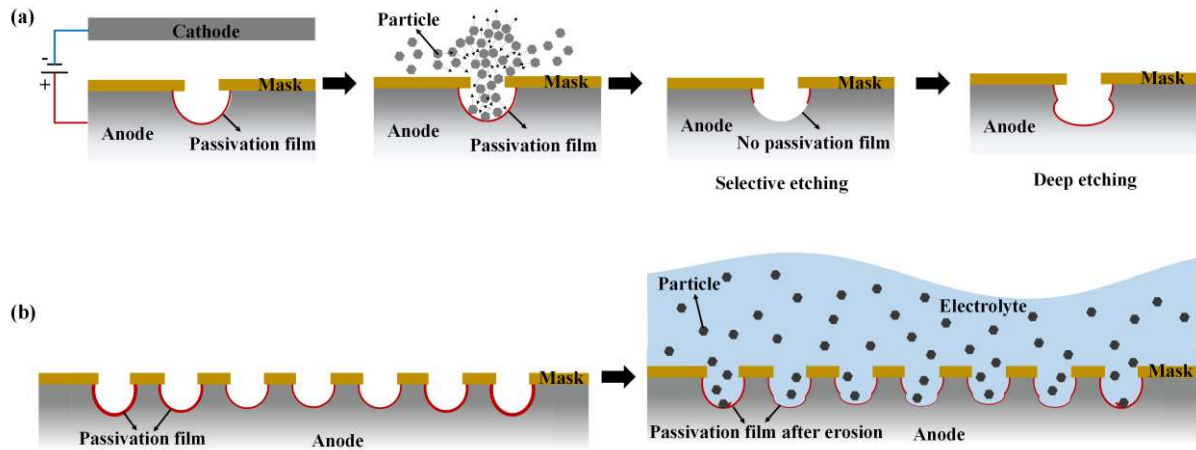


Fig. 1 Principle diagram of PA-TMEE: **a** effect of PA-TMEE on localization; **b** effect of PA-TMEE on uniformity

2.2 Theoretical analysis

TMEE is a complicated process because the electrochemical reaction is affected by a lot of physical parameters. It is well known that the machining precision of TMEE depends strongly on both the conductivity of the electrolyte and the film resistance of the anode [23, 24]. In contrast to TMEE, the particles significantly affected the conductivity of the electrolyte and the film resistance of the anode in PA-TMEE. Therefore, the theoretical analysis focuses on the effect of particles in this paper. To realize the coupling between the particles and the electric field, we use the reaction model as shown in Fig. 2. The electrolyte drives the particles to erode the surface of the anode continuously. On the one hand, introducing particles reduces the electrolyte's electrical conductivity. On the other hand, particle erosion decreases the film resistance of the passive film on the anode. Both will affect the current density. Finally, PA-TMEE was simulated using flow field, particle tracking, electric current and deformed geometry models.

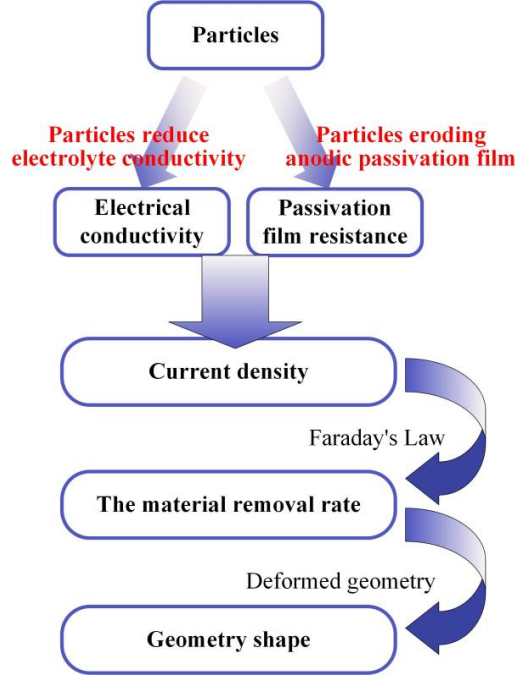


Fig. 2 Basic principle of the reaction model

2.2.1 Flow field model

During electrochemical etching, cathode and anode produce gas and metal ions, respectively. Thus, the electrochemical system was viewed as a gas-liquid two-phase flow model. The Navier-Stokes equation can describe it as:

$$\rho_1 \frac{\partial \mathbf{u}_1}{\partial t} + \rho_1 (\mathbf{u}_1 \cdot \nabla) \mathbf{u}_1 = \nabla \cdot [-p\mathbf{I} + \mu(\nabla \mathbf{u}_1 + (\nabla \mathbf{u}_1)^T)] + \phi_1 \rho_1 \mathbf{g} + \mathbf{F} \quad (4)$$

$$\rho_1 \nabla \cdot \mathbf{u}_1 = 0 \quad (5)$$

Where ρ_1 is the electrolyte density, μ is the dynamic viscosity of the electrolyte, \mathbf{u}_1 is the flow velocity, p is the pressure, ϕ_1 is the volume fraction of the liquid phase, and \mathbf{F} is the volume force.

The gas phase transport equation is:

$$\frac{\partial \phi_g \rho_g}{\partial t} + \nabla \cdot \phi_g \rho_g \mathbf{u}_g = -m_{gl} \quad (6)$$

Where \mathbf{u}_g is the gas phase velocity, ϕ_g is the volume fraction of gas phase, and m_{gl} is the mass

transfer rate from the gas to the liquid.

2.2.2 Particle tracking model

In this paper, the particle tracking model was used to simulate the motion and force of SiC particles. The particle tracking model allows for excellent controlling particle properties and coupling with the flow field. The electrolyte with SiC particles continuously eroded the surface of the anode micro pits. Newton's second law controlled the motion of SiC particles in fluids:

$$\frac{d(\mathbf{m}\mathbf{u})}{dt} = \mathbf{F}_t \quad (7)$$

where \mathbf{u} is the velocity of the particle, m is the mass of the particle, and \mathbf{F}_t is the total force.

The Finnie erosion model [25] was used to calculate the quality of the erosion of SiC particles on the surface of the anode micro pits.

$$\Delta m = \sum_i \frac{c_i \rho m \mathbf{u}_i^2}{4p(1+mr^2/I)} F(\alpha_i) \quad (8)$$

$$F(\alpha_i) = \begin{cases} \cos^2 \alpha & \tan \alpha_i > \frac{P}{2} \\ \frac{2}{P} \left[\sin(2\alpha_i) - \frac{2}{P} \sin^2 \alpha_i \right] & \tan \alpha_i < \frac{P}{2} \end{cases} \quad (9)$$

$$P = \frac{K}{1+mr^2/I} \quad (10)$$

where i is the i -th particle, Δm is the total mass of eroding particles, c is the particle ratio for ideal cutting, p is the Vickers hardness of the metal, m is the mass of a single particle, r is the average particle radius, I is the rotational inertia of the particle, α is the angle of incidence, P is a dimensionless parameter, K is the ratio of the vertical force of the particle to the horizontal force.

The anode passivation film was assumed to be a cylinder of equal cross-sectional area perpendicular to the electric field direction. Then, the resulting eroding mass Δm was combined with

Ohm's law $R = \sigma L/S$ to calculate the change in resistance of the passivation film after eroding of the SiC particles as:

$$\Delta R_f = \frac{\sigma * \Delta m}{\rho_{\text{anode}} S^2} \quad (11)$$

ΔR_f is the amount of change in resistance of the passivation film, σ is the resistivity of the passivation film, and ρ_{anode} is the density of the anode metal, and S is the cross-sectional area of the electrolysis product perpendicular to the direction of the electrical field.

2.2.3 Electric current model

During electrochemical etching, the change in conductivity of the electrolyte causes a change in the electric field. A constant temperature water bath will control the electrolyte temperature. Therefore, the effect of temperature on the conductivity is neglected. The change in conductivity is shown in equation (12) [26]:

$$\kappa = \kappa_0 * (1 - \beta)^n \quad (12)$$

Where κ_0 is the initial conductivity, β is the volume fraction of the insulation in the electrolyte, $\beta = \phi_g + \phi_p$, ϕ_g and ϕ_p represent the volume fraction of gases and the volume fraction of particles, respectively. n is the Bruggeman coefficient.

The change in electrolyte conductivity will cause a change in the electric field, which is related as follows:

$$\mathbf{i}_e = \kappa * \nabla \Phi \quad (13)$$

where \mathbf{i}_e is the current density and Φ is the total voltage.

Since a passivation film will be formed at the interface between electrode and electrolyte, leading to additional voltage loss.

$$\Delta\Phi_f = \mathbf{i}(R_f - \Delta R_f) \quad (14)$$

where $\Delta\Phi_f$ is the potential drop generated by the passivation film, \mathbf{i} is the total current, and R_f is the initial film resistance.

Equation (13) can become:

$$\mathbf{i}_e = \kappa * \nabla(\Phi - \mathbf{i}(R_f - \Delta R_f)) \quad (15)$$

The anode dissolution velocity can be concluded from Faraday's law as shown in equation (16):

$$v = \frac{M * \mathbf{i}_e}{\rho_{\text{anode}} z F_0} \quad (16)$$

Where v is the anode dissolution rate, M and ρ_{anode} is the molar mass and density of the anode metal, respectively. z is the volumetric electrochemical equivalent of the material, and F_0 is the Faraday constant.

The above theoretical analysis shows that SiC particles can affect the conductivity of the electrolyte and anode film resistance, which consequently affects electrochemical machining. On the one hand, the addition of particles decreases the conductivity of the electrolyte, thus reducing lateral corrosion. On the other hand, the selective etching of particles on the passivation can reduce the anode film resistance and improve the etching depth. So simulations and experimental validation are carried out in this paper.

2.3 Model building and simulation conditions

A coupled multi-physical field model was developed to study the effect of particles on TMEE, which contains a flow field model, an electrochemical model, and a particle motion model. COMSOL Multiphysics (COMSOLAB, Stockholm, Sweden) was employed to couple and analyze all models. Fig. 3 depicts a simple two-dimensional model for the multi-physics field calculation. The anode was

304 stainless steel, and the cathode was a carbon plate. The length L of the cathode and anode was 80 mm. The distance T_1 between the cathode and the mask was 26.994mm. The thickness of the mask T_2 was 0.006mm. The mask had uniformly distributed penetration holes with the characteristic size l of 0.1 mm. The 100 g/L NaNO_3 and 10 g/L NaCl electrolyte with 40 μm SiC particles flowed from the inlet to the outlet at 0.8 m/s. The parameters of the simulation are shown in Table 1. The following assumptions were used to simplify the model:

- (1) The electrolyte had a constant dynamic viscosity [27].
- (2) The interactions between SiC particles were not considered [28].

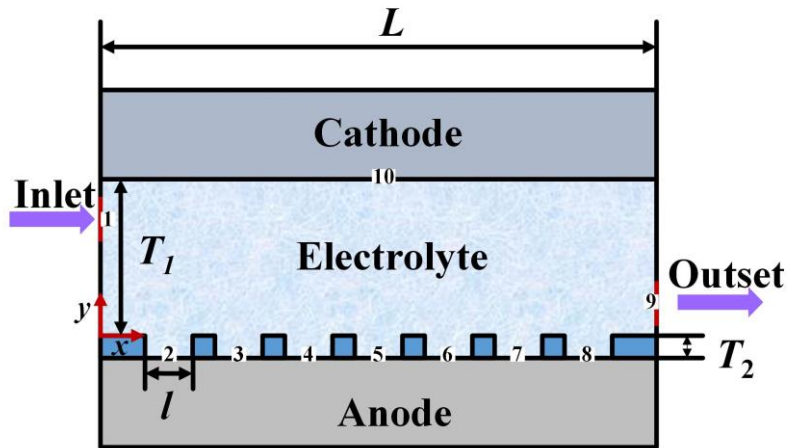


Fig. 3 PA-TMEE model for multi-physical field simulation

Table 1 Parameters of the simulation

Simulation parameters	Value
Dynamic viscosity of the electrolyte, μ	$1.004 \times 10^{-3} \text{Pa} \cdot \text{s}$
Electrolyte density, ρ	1100kg/m^3
Electrolyte temperature, T	298K
Application Voltage, U	10V
Machining time, t	60s
Initial conductivity, κ_0	10S/m
Number of particles, n	3000

2.4 Simulation results

Fig. 4 shows the spatial distribution of SiC particles in the PA-TMEE. The SiC particles impact the micro pits and walls under the combined gravity and electrolyte. The erosion of SiC particles promotes the directional removal of the passivation film on the micro pits. Fig. 5 shows the distribution of the average erosion mass caused by SiC particles eroding the surface of micro pits. The erosion of SiC particles affects the central region of the anode significantly more than the edges. Fig. 6 compares the profiles change of micro pits with and without particles. In traditional TMEE, the dimension of the micro pits varies with the position. In contrast, in PA-TMEE, the dimension of each micro pit is almost the same regardless of the position, which means that the micro pits array has excellent uniformity. The CV_{diameter} of the micro pits was reduced from 7.3% to 2.4%, and the CV_{depth} from 12.5% to 4.3%.

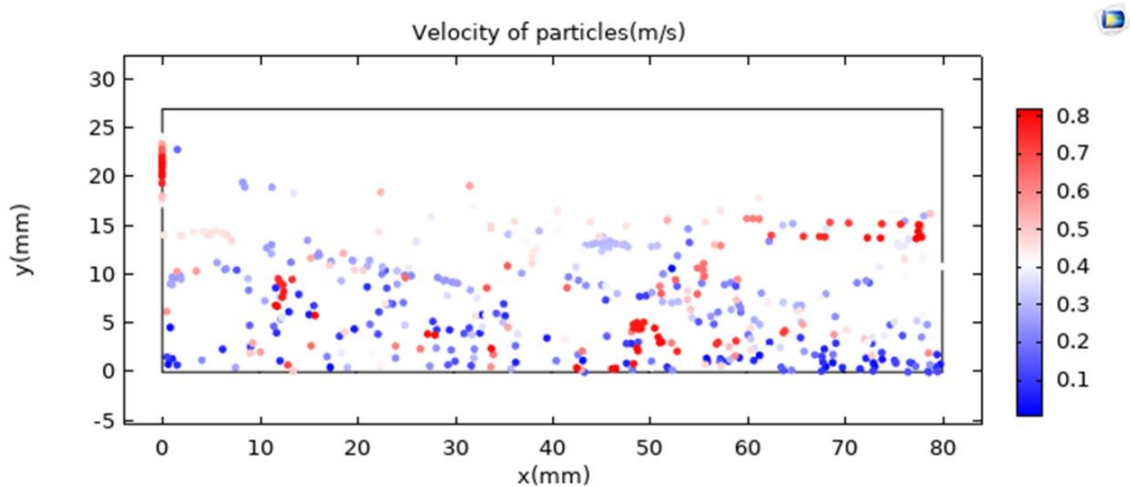


Fig. 4 The spatial distribution of SiC particles in the PA-TMEE

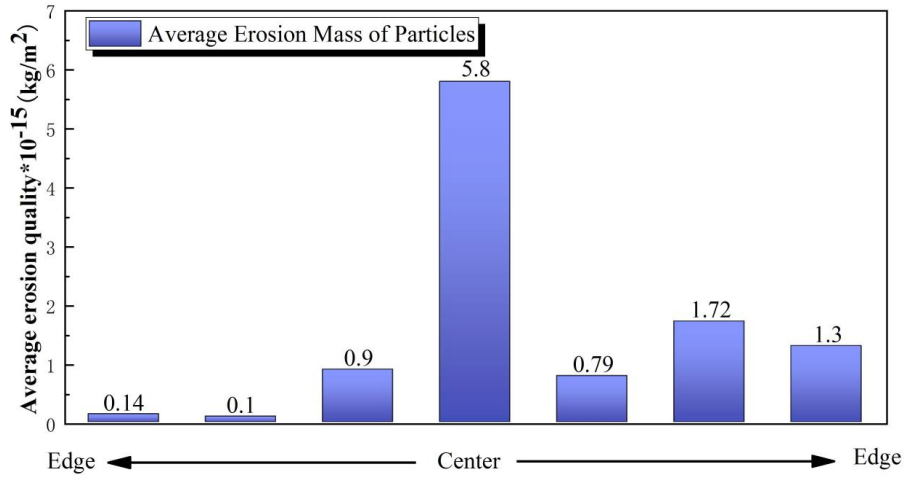


Fig. 5 Average erosion mass distribution of SiC particles on the surface of the micro pits

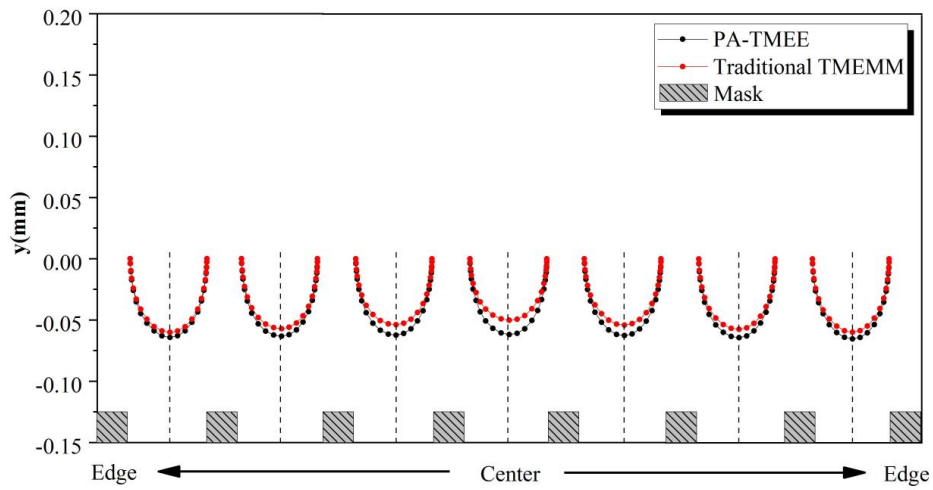


Fig. 6 Comparison of anode profiles with PA-TMEE and traditional TMEE

Fig. 7 shows the profiles of a micro pit at the center of the workpiece with TMEE and PA-TMEE.

The average etching diameter and depth of traditional TMEE were 172.1 μm and 50.1 μm , respectively.

The EF of micro pits was 1.4. After particle erosion, the average etching diameter of the micro pits

reduced to 152.8 μm , and the average etching depth increased to 61.8 μm with an EF of 2.3. These

findings suggest that, from a simulation perspective, particle erosion facilitates improved localization

of micro pits.

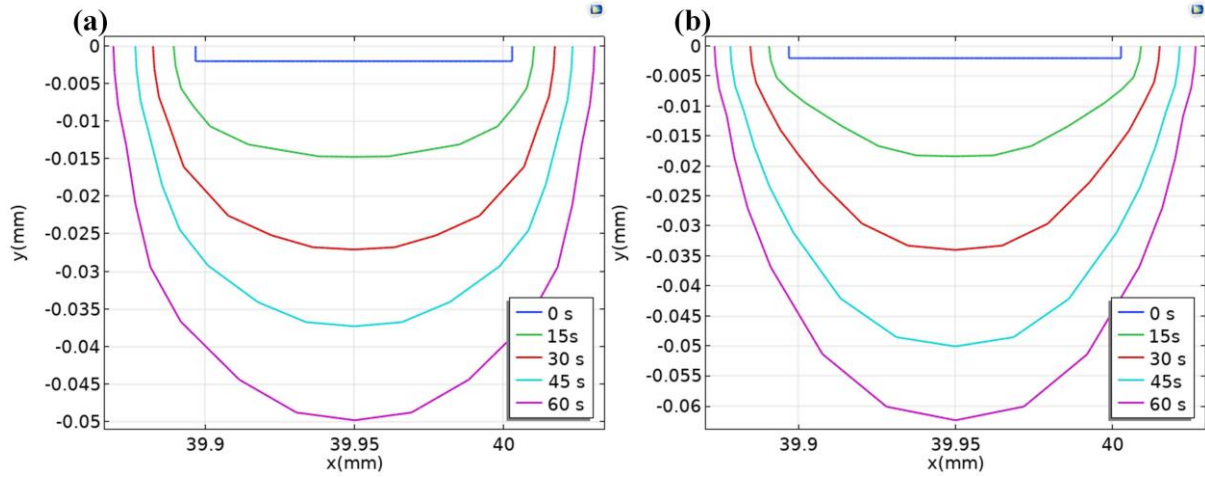


Fig. 7 Comparison of single micro pit profile with different machining methods: **a** traditional TMEE; **b** PA-TMEE

3 Experiment

PA-TMEE experiments were to verify the effect of particles on the localization and uniformity of electrochemical machining. Firstly, polished 304 stainless steel was used as the substrate and cleaned in an ultrasonic cleaner with acetone and ethanol. Then, the mask was used as a BN303 photoresist with 100 μm diameter micro pits. The fabrication of the mask includes photoresist coating, pre-baking, exposure, photoresist development, and post-baking. Fig. 8 shows the designed PA-TMEE device used for all experiments in this paper. The designed PA-TMEE device mainly consisted of fastening screws, conductive screws, cathode clamps, and anode clamps. Graphite was used as a cathode conducting material. 100 g/L NaNO_3 and 10 g/L NaCl were adopted as electrolytes due to their low cost, good availability, and relatively low toxicity. During the PA-TMEE, the particles were driven by an electrolyte pump. A comparative experiment between TMEE and PA-TMEE was carried out to verify the effect of particles. The specific experimental parameters are shown in Table 2. The profiles of the micro pits were characterized by STM7 (OLYMPUS) microscopic.

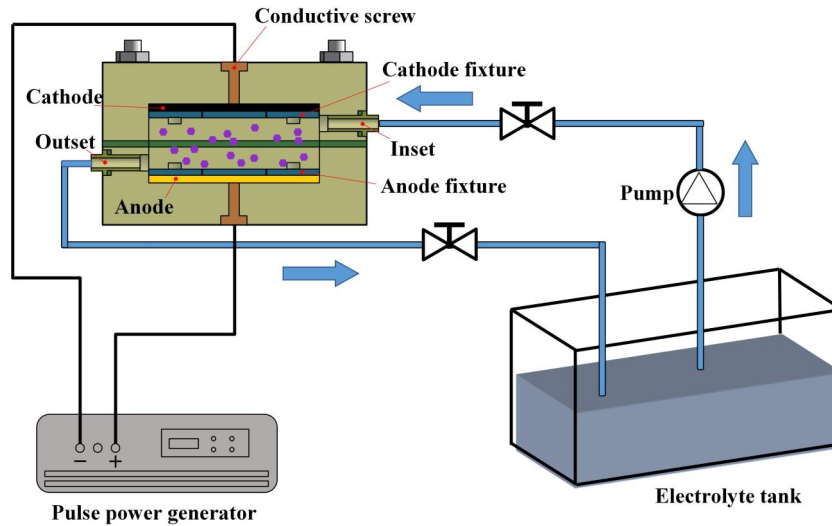


Fig. 8 The schematic view of PA-TMEE

Table 2 Parameters of the etching experiments

Experiments	Experiment1	Experiment2
Comparison experiments	Traditional TMEE	PA-TMEE
Dispersion phase		SiC, 4 g/L, particle diameter 40 μm
Application voltage	10V	10V
Etching time	60s	60s
Flow rate	3L/min	3L/min
Electrolyte temperature	30°C	30°C

4 Results and discussion

4.1 Comparative analysis of traditional TMEE and PA-TMEE

Fig. 9 shows the produced micro pits by TMEE and PA-TMEE. It can be seen that a uniform micro pits array can be produced using PA-TMEE. Ten test points were selected along A-A and B-B, respectively. Fig. 10(a) shows the measuring results. The average diameter of micro pits was 154 μm , and the average depth was 55.7 μm in PA-TMEE. The average etching micro pits diameter was 168.1

μm , and the average etching depth was $51.7 \mu\text{m}$ in TMEE. EF improved from 1.5 to 2.1 with particles. CV_{diameter} decreased from 8.3% to 3.7%, and CV_{depth} decreased from 14.4% to 5.4% with particles. The results showed that PA-TMEE improves the uniformity and localization of the micro pits. Meanwhile, Fig. 10(b) compares the experimental and simulated etching dimensions in the PA-TMEE method. The results show that the simulation errors of etching diameter and etching depth are 0.78% and 10.95%, respectively.

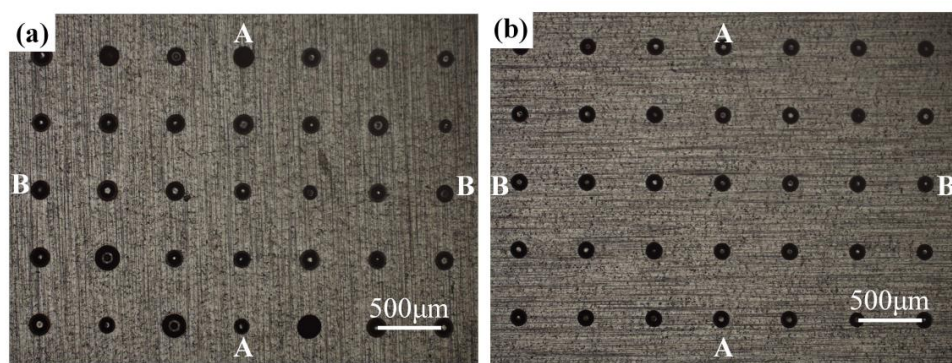


Fig. 9 Comparison of electrochemical etching results: **a** traditional TMEE; **b** PA-TMEE (A-A and B-B are the selected directions of the test points)

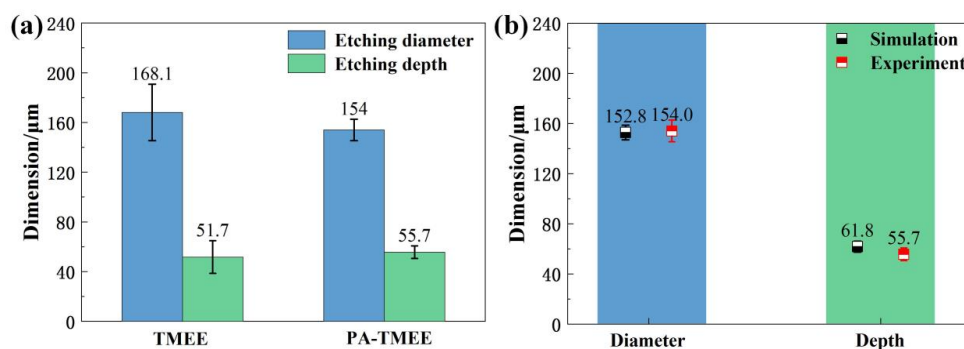


Fig. 10 Comparison of etching results: **a** comparison of etching diameter and etching depth for different machining methods; **b** comparison of simulated and experimental results of PA-TMEE

4.2 Effect of particles on PA-TMEE

4.2.1 Effect of particle diameter on PA-TMEE

In PA-TMEE, the diameter of the particles significantly influences the machining. When the diameter of the particle is too large, it is difficult to erode the bottom of the micro pits. Smaller particles will erode the bottom of the micro pits and the lateral areas of the micro pits. Therefore, a suitable particle diameter can improve the machining precision of micro pits. Fig. 11 shows the dimensions of the micro pits with different particle diameters.

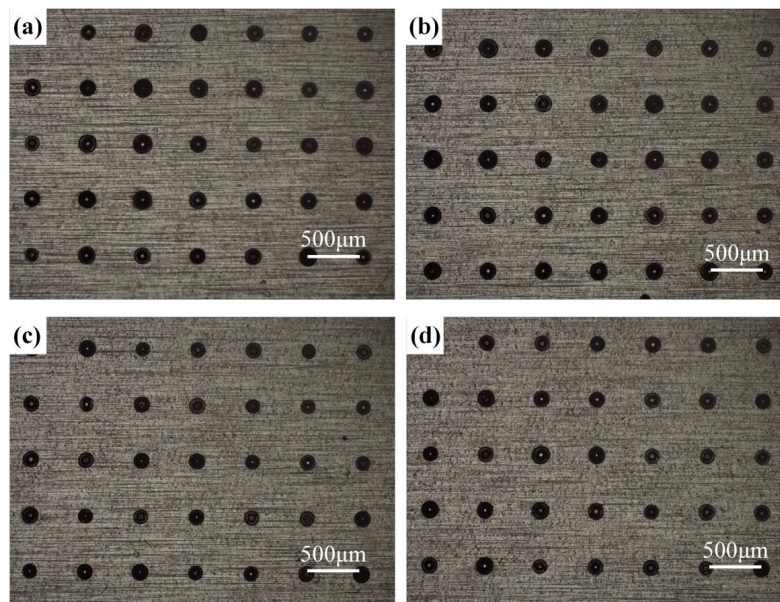


Fig. 11 Etching of micro pits with SiC particles of different diameters: **a** 10 μm ; **b** 20 μm ; **c** 40 μm ; **d** 60 μm

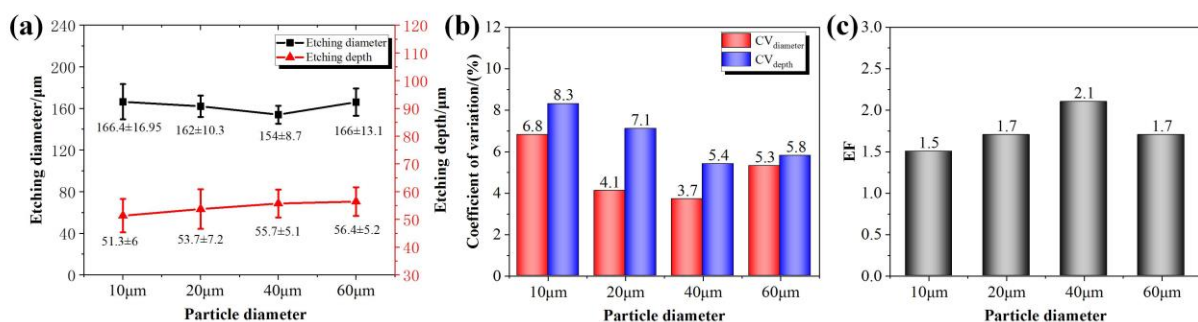


Fig. 12 Micro pits etched results with different particle diameters: **a** diameter and depth of micro pits;

b CV value of micro pits diameter and depth; **c** EF of micro pits

The experimental results showed that the average diameter of the micro pits decreased from 166.4 μm to 154 μm . The average depth of the micro pits increased from 51.3 μm to 55.7 μm when the particle diameter increased from 10 μm to 40 μm . When the average diameter of the particles was increased to 60 μm , the diameter and depth of the micro pits were 166 μm and 56.4 μm , respectively. The increased depth of the micro pits is attributed to the ability of particle erosion. Fig. 12 shows the statistical results of EF and CV values with different particle diameters. It can be seen that among the selected particle diameters, when the particle diameter was 40 μm , the micro pits had the best localization and uniformity. The EF was 2.1. The $\text{CV}_{\text{diameter}}$ and CV_{depth} of micro pits were 3.7% and 5.4%, respectively.

4.2.2 Effect of particle content on PA-TMEE

Particle content is also one of the critical parameters in PA-TMEE. PA-TMEE with different particle contents was studied at the same voltage and 40 μm particles. Fig. 13 shows the etching results obtained for particle contents 2 g/L to 8 g/L. The experimental results showed that when the particle content increased from 2 g/L to 6 g/L, the average diameter of the micro pits decreased from 158.3 μm to 148.7 μm . The average depth of the micro pits increased from 53.3 μm to 58 μm . However, when the particle content was increased to 8 g/L, the average diameter of the micro pits was 153.1 μm , and the average depth of the micro pits was 52.1 μm . The conductivity of the electrolyte can explain the decrease in etching. A conductivity meter was used to measure the conductivity in this paper. The test results are shown in Table 3. The conductivity of the electrolyte decreased with increasing particle content. The EF and CV of the micro pits at different particle contents are shown in Fig. 14. The maximum EF of the micro-pits was 2.4 at a particle content of 6 g/L. When the particle content

increased from 2 g/L to 8 g/L, the CV_{diameter} was 4.7%, 3.7%, 3.3%, and 4.4%, respectively. The CV_{depth} was 6.7%, 5.4%, 5.2% and 6.9%. The best localization and uniformity of micro pits on metal surfaces were achieved in the experiments with a particle content of 6 g/L.

Table 3 The conductivity of electrolytes with different particle content

Particle content	2 g/L	4 g/L	6 g/L	8 g/L
Electrolyte conductivity	134.5 mS/cm	132.7 mS/cm	129.8 mS/cm	127.9 mS/cm

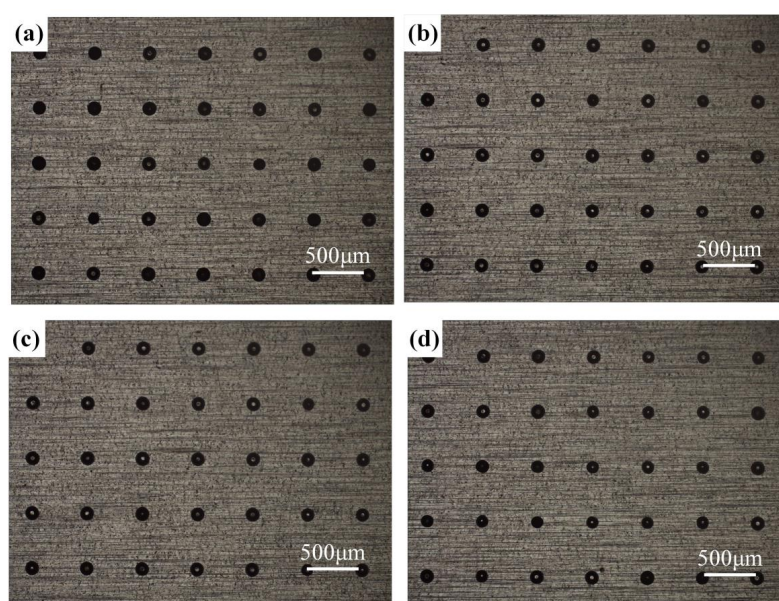


Fig. 13 Micro pits etching profiles at different 40 μm particle content: **a** 2 g/L; **b** 4 g/L; **c** 6 g/L; **d** 8 g/L

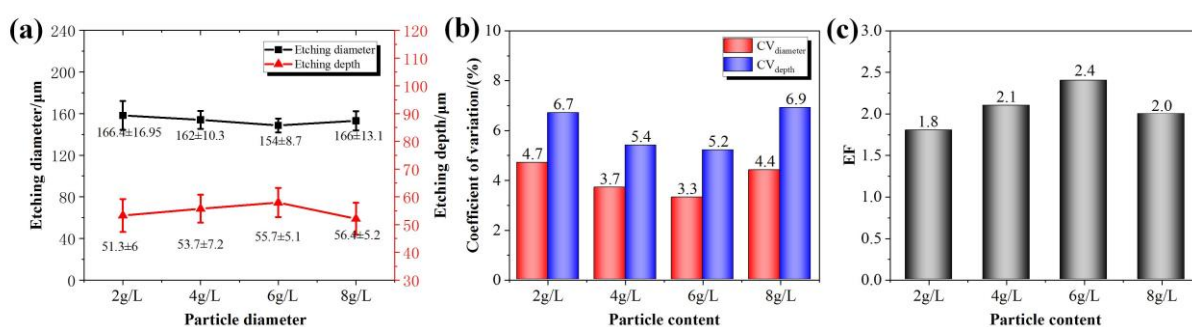


Fig. 14 Micro pits etching results with different particle content: **a** diameter and depth of micro pits; **b** CV value of micro pits diameter and depth; **c** EF of micro pits

5 Analysis of the machining mechanism of PA-TMEE

This paper used a combination of SEM and EDS to analyze the machining mechanism of PA-TMEE. Fig. 15 shows the micro pits at the center of the substrate by TMEE and PA-TMEE machining. 40 μm , 6 g/L SiC particles were used for PA-TMEE experiments, and other parameters are shown in Table 2. Comparing Fig. 15 (a) and (b), it can be seen that cracks appear on the surface of the micro pits prepared by PA-TMEMM. The cracks may be caused by plastic deformation caused by particles eroding the surface of the micro pits.

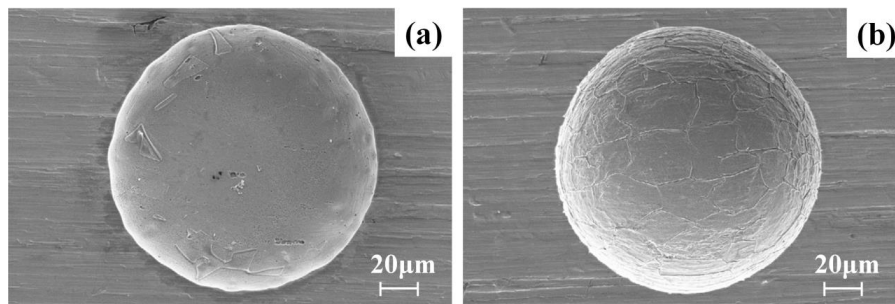


Fig. 15 Profiles of micro pits for different machining methods: **a** traditional TMEE; **b** PA-TMEE

To confirm the synergistic effect of particles and TMEE, EDS was used to analyze the effect of particles on TMEE. Fig. 16(b) and Fig. 16(c) show the results of EDS analysis of region 1 and region 2 in TMEE machining, respectively. The oxygen of the two regions was 7.08% and 7.63%, respectively. The experimental results showed that passivation generated an oxide layer on the surface of the micro pit. Similarly, the EDS analysis of a micro pit surface machined by PA-TMEE is shown in Fig. 17. Notably, the oxygen in region 2 was 6.57%, while in region 1 was only 3.56%. Region 1 is dominantly exposed to the particles-TMEE interaction zone compared to region 2. The experimental results showed that the passivation film in the center of the micro pits is weakened by the particles, which indicates that the particles have a selective erosion on the surface of the micro pits. Therefore, two material removal mechanisms exist on the surface of the micro pit shown in Fig. 17(a), namely

electrochemical dissolution based on Faraday's law and particle erosion under the electrolyte flow field.

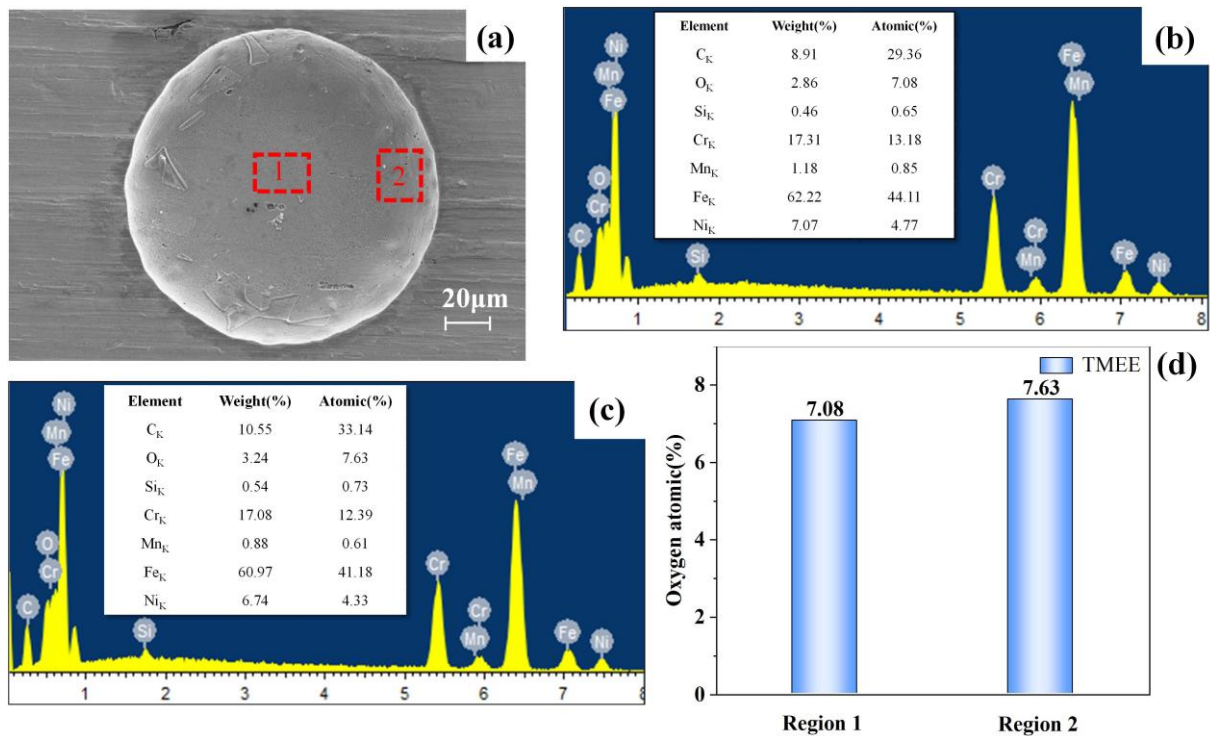


Fig. 16 **a** SEM image of the micro pit machined with TMEE; **b** EDS analysis of region 1; **c** EDS analysis of region 2; **d** comparison of the oxygen in regions 1 and 2

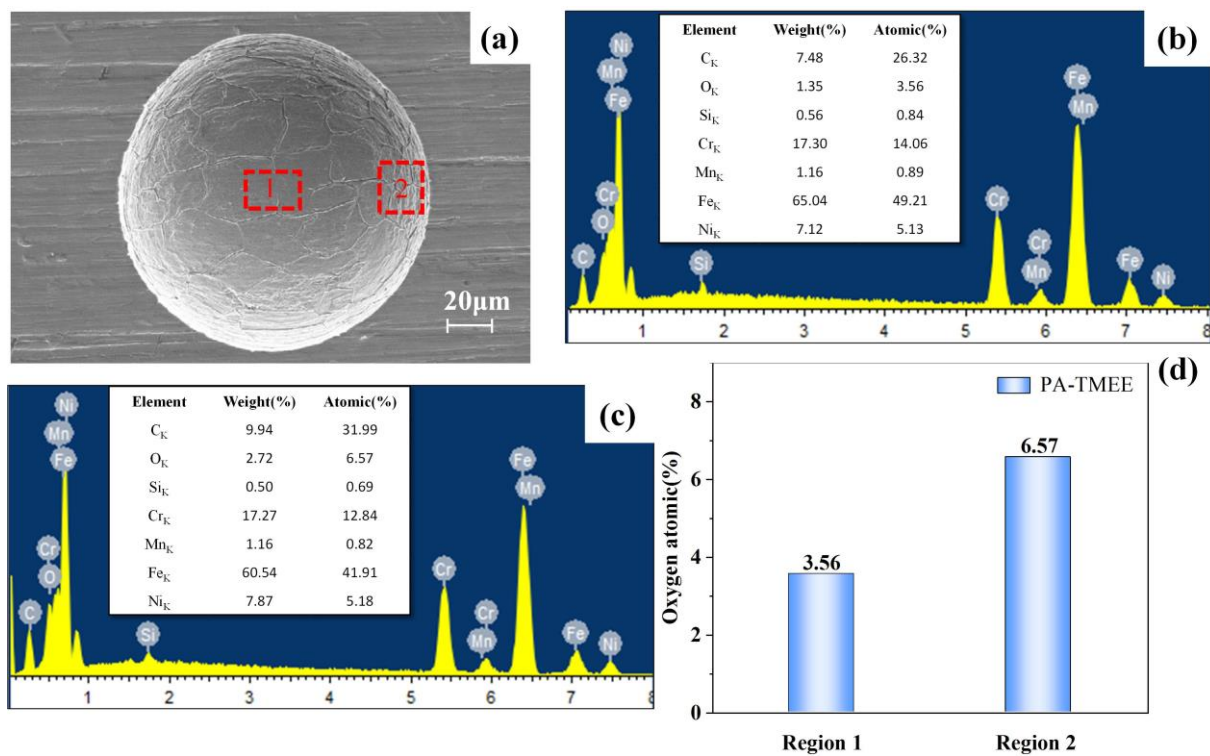


Fig. 17 **a** SEM image of the micro pit machined with PA-TMEE; **b** EDS analysis of region 1; **c** EDS

analysis of region 2; **d** comparison of the oxygen in regions 1 and 2

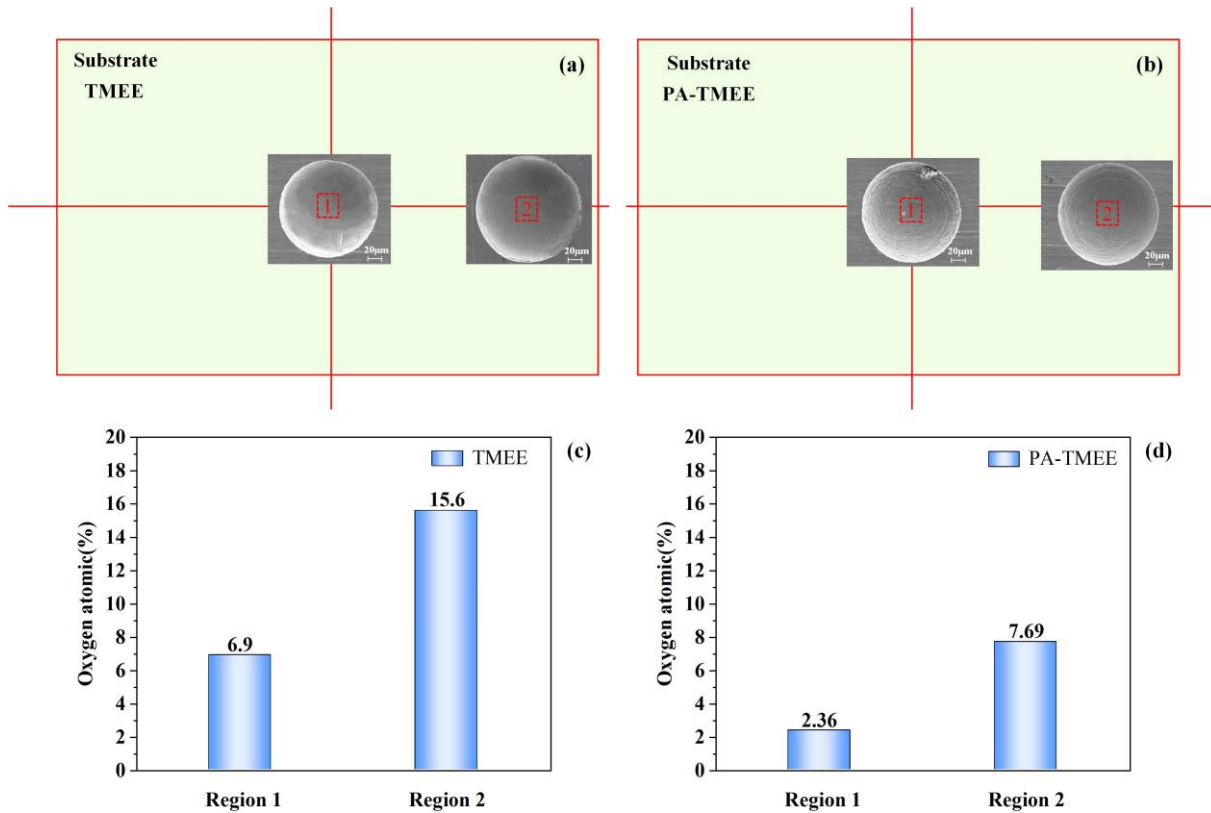


Fig. 18 a SEM image of the micro pits at the center and edge of the substrate obtained by TMEE; **b** SEM image of the micro pits at the center and edge of the substrate obtained by PA-TMEE; **c** the oxygen content of regions 1 and 2 in TMEE; **d** the oxygen content of regions 1 and 2 in PA-TMEE

The oxygen at the same locations of different micro pits on the substrate was compared and analyzed to clarify the effectiveness of PA-TMEE for machining uniformity of large-area micro pits array. Fig. 18(a, b) shows the SEM images of the micro pits in the center and edge of the substrate in TMEE and PA-TMEE, respectively. The oxygen of region 1 and region 2 in TMEE is shown in Fig. 18 (c). The oxygen of region 2 was 15.6%, while region 1 was only 6.9%, a difference of 8.7%. This difference is mainly due to the non-uniform distribution of the passivation film caused by the electric field edge effect. The edge effect of the electric field leads to more material removal from the micro pits at the edges of the substrate, which leads to more passivation film. The oxygen of regions 1 and

2 in PA-TMEE is shown in Fig. 18 (d). The oxygen content of the micro pits at region 1 and region 2 was 2.36% and 7.69%, respectively, with a difference of 5.33%. Compared with the micro pits machined by TMEE, the non-uniform distribution of the passivation film is improved in the PA-TMEE process, which facilitates the uniformity of the large-area micro pits array.

6 Conclusion

This paper proposes the PA-TMEE method to improve the machining precision of deep microstructures. The main conclusions can be summarized as follows:

(1) A multi-physics field coupling model of the electric field, flow field, and particle motion simulated the PA-TMEE machining experiment. The simulation results showed that the erosion of particles could enhance uniformity and localization.

(2) The results of the comparison experiment showed that compared to the TMEE method, the PA-TMEE method could enhance the EF from 1.5 to 2.1. CV_{diameter} decreased from 8.3% to 3.7%, and CV_{depth} decreased from 14.4% to 5.4%.

(3) When SiC particles with a diameter of 40 μm and a content of 6 g/L were applied, micro pits of 148.7 μm average diameter and 58.0 μm average depth were obtained. The EF of the micro pits was 2.4, and CV_{diameter} and CV_{depth} were 3.3% and 5.2%, respectively.

(4) The oxygen content of the surface was taken as an indicator for the passivation film. SEM and EDS analysis results showed that the material removal of PA-TMEE differs from an exclusively TMEE process. The electrochemical etching and particle erosion in the PA-TMEE method facilitate the machining precision of deep micro pits array.

Funding

This work was supported by the National Natural Science Foundation of China (No. 51975103) and Dalian Science & Technology Innovation Fund (2020JJ25CY018).

Availability of data and material

Yes, the data and material are available.

Code availability

Not applicable.

Declarations

Ethics approval Not applicable.

Consent to participate Not applicable.

Consent for publication Not applicable.

Competing interests The authors declare no competing interests.

Author contribution

Liqun Du: Conceptualization, Methodology, Data curation, Funding acquisition. Mingxin Yu: Investigation, Validation, Writing - original draft, Writing - review & editing. Ke Zhai: Writing - review & editing. Kunming Zheng: Supervision. Haohao Cheng: Supervision, Formal analysis. Shuxuan Wang: Supervision, Writing - review & editing. Junshan Liu: Supervision.

References

1. Gachot C, Rosenkranz A, Hsu SM, Costa HL, (2017) A critical assessment of surface texturing for friction and wear improvement. *Wear* 372-373: 21-41.

<https://doi.org/10.1016/j.wear.2016.11.020>.

2. Cho M, (2016) Friction and wear of a hybrid surface texturing of polyphenylene sulfide-filled micropores. *Wear* 346-347: 158-167.

<https://doi.org/10.1016/j.wear.2015.11.010>.

3. Qu J, Xu HB, Feng ZL, Frederick DA, An LA, Heinrich H, (2011) Improving the tribological characteristics of aluminum 6061 alloy by surface compositing with sub-micro-size ceramic particles via friction stir processing. *Wear* 271: 1940-1945.

<https://doi.org/10.1016/j.wear.2010.11.046>.

4. Shen XH, Tao GC, (2015) Tribological behaviors of two micro textured surfaces generated by vibrating milling under boundary lubricated sliding. *Int J Adv Manuf Tech* 79: 1995-2002.

<https://doi.org/10.1007/s00170-015-6965-x>.

5. Li DX, Chen XX, Guo CH, Tao J, Tian CX, Deng YM, Zhang WW, (2017) Micro surface texturing of alumina ceramic with nanosecond laser. *Procedia Engineer* 174: 370-376.

<https://doi.org/10.1016/j.proeng.2017.01.155>.

6. Wu X, Li L, He N, Zhao GL, Shen JY, (2019) Investigation on the surface formation mechanism in micro milling of cemented carbide. *International Journal of Refractory Metals & Hard Materials* 78: 61-67.

<https://doi.org/10.1016/j.ijrmhm.2018.09.001>.

7. Wang H, Chi GX, Wang YK, Yu FX, Wang ZL, (2019) Fabrication of superhydrophobic metallic surface on the electrical discharge machining basement. *Appl Surf Sci* 478: 110-118.
<https://doi.org/10.1016/j.apsusc.2019.01.102>.
8. Zhai K, Du L, Wen Y, Wang S, Cao Q, Zhang X, Liu J, (2020) Fabrication of micro pits based on megasonic assisted through-mask electrochemical micromachining. *Ultrasonics* 100: 105990.
<https://doi.org/10.1016/j.ultras.2019.105990>.
9. Chen XL, Qu NS, Li HS, Xu ZY, (2015) Pulsed electrochemical micromachining for generating micro-dimple arrays on a cylindrical surface with a flexible mask. *Appl Surf Sci* 343: 141-147.
<https://doi.org/10.1016/j.apsusc.2015.03.087>.
10. Saxena KK, Qian J, Reynaerts D, (2018) A review on process capabilities of electrochemical micromachining and its hybrid variants. *Int J Mach Tool Manu* 127: 28-56.
<https://doi.org/10.1016/j.ijmachtools.2018.01.004>.
11. Landolt D, Chauvy PF, Zinger O, (2003) Electrochemical micromachining, polishing and surface structuring of metals: fundamental aspects and new developments. *Electrochim Acta* 48: 3185-3201.
[https://doi.org/10.1016/S0013-4686\(03\)00368-2](https://doi.org/10.1016/S0013-4686(03)00368-2).
12. Qian SQ, Ji F, Qu NS, Li HS, (2014) Improving the Localization of Surface Texture by Electrochemical Machining with Auxiliary Anode. *Materials and Manufacturing Processes* 29: 1488-1493.
<https://doi.org/10.1080/10426914.2014.930950>.
13. Chen XL, Qu NS, Li HS, (2015) Improvement of dimensional uniformity on micro-dimple arrays generated by electrochemical micro-machining with an auxiliary electrode. *Int J Adv Manuf Tech* 80: 1577-1585.

<https://doi.org/10.1007/s00170-015-7147-6>.

14. Zhang XF, Qu NS, Chen XL, (2016) Sandwich-like electrochemical micromachining of micro-dimples. *Surf Coat Tech* 302: 438-447.

<https://doi.org/10.1016/j.surfcoat.2016.05.088>.

15. Zhang XF, Qu NS, Fang XL, (2017) Sandwich-like electrochemical micromachining of micro-dimples using a porous metal cathode. *Surf Coat Tech* 311: 357-364.

<https://doi.org/10.1016/j.surfcoat.2017.01.035>.

16. Pan YQ, Hou ZB, Qu NS, (2019) Improvement in accuracy of micro-dimple arrays prepared by micro-electrochemical machining with high-pressure hydrostatic electrolyte. *Int J Adv Manuf Tech* 100: 1767-1777.

<https://doi.org/10.1007/s00170-018-2822-z>.

17. Kim Y, Youn S, Cho YH, Park H, Chang BG, Oh YS, (2011) A multi-step electrochemical etching process for a three-dimensional micro probe array. *J Micromech Microeng* 21(1): 015019.

<https://doi.org/10.1088/0960-1317/21/1/015019>.

18. Mineta T, (2004) Electrochemical etching of a shape memory alloy using new electrolyte solutions. *J Micromech Microeng* 14: 76-80.

<https://doi.org/10.1088/0960-1317/14/1/310>.

19. Chauvy PF, Hoffmann P, Landolt D, (2003) Applications of laser lithography on oxide film to titanium micromachining. *Appl Surf Sci* 208: 165-170.

[https://doi.org/10.1016/S0169-4332\(02\)01361-2](https://doi.org/10.1016/S0169-4332(02)01361-2).

20. Baldhoff T, Nock V, Marshall AT, (2018) Review-Through-Mask Electrochemical Micromachining. *J Electrochem Soc* 165: E841-E855.

<https://doi.org/10.1149/2.1341814jes>.

21. Qu NS, Chen XL, Li HS, Zeng YB, (2014) Electrochemical micromachining of micro-dimple arrays on cylindrical inner surfaces using a dry-film photoresist. *Chinese J Aeronaut* 27: 1030-1036.

<https://doi.org/10.1016/j.cja.2014.03.012>.

22. Ming PM, Zhao CH, Zhang XM, Li XC, Qin G, Yan L, (2018) Investigation of foamed cathode through-mask electrochemical micromachining developed for uniform texturing on metallic cylindrical surface. *Int J Adv Manuf Tech* 96: 3043-3056.

<https://doi.org/10.1007/s00170-018-1755-x>.

23. Jain VK, Chouksey AK, (2018) A comprehensive analysis of three-phase electrolyte conductivity during electrochemical macromachining/micromachining. *P I Mech Eng B-J Eng* 232: 2449-2461.

<https://doi.org/10.1177/0954405417690558>.

24. Schultze JW, Lohrengel MM, (2000) Stability, reactivity and breakdown of passive films. Problems of recent and future research. *Electrochim Acta* 45: 2499-2513.

[https://doi.org/10.1016/S0013-4686\(00\)00347-9](https://doi.org/10.1016/S0013-4686(00)00347-9).

25. Finnie I, (1995) Some Reflections on the Past and Future of Erosion. *Wear* 186: 1-10.

[https://doi.org/10.1016/0043-1648\(95\)07188-1](https://doi.org/10.1016/0043-1648(95)07188-1).

26. Wang JY, Xu JW, (2001) Principle and application of electrochemical machining. China Machine Press (In Chinese)

27. Fang XL, Qu NS, Zhang YD, Xu ZY, Zhu D, (2014) Effects of pulsating electrolyte flow in electrochemical machining. *J Mater Process Tech* 214: 36-43.

<https://doi.org/10.1016/j.jmatprotec.2013.07.012>.

28. Sharma MK, Suru A, Joshi A, Kulkarni AA, (2020) A Novel Flow Reactor for Handling

Suspensions: Hydrodynamics and Performance Evaluation. Industrial & Engineering Chemistry

Research 59: 16462-16472.

<https://doi.org/10.1021/acs.iecr.9b06864>.

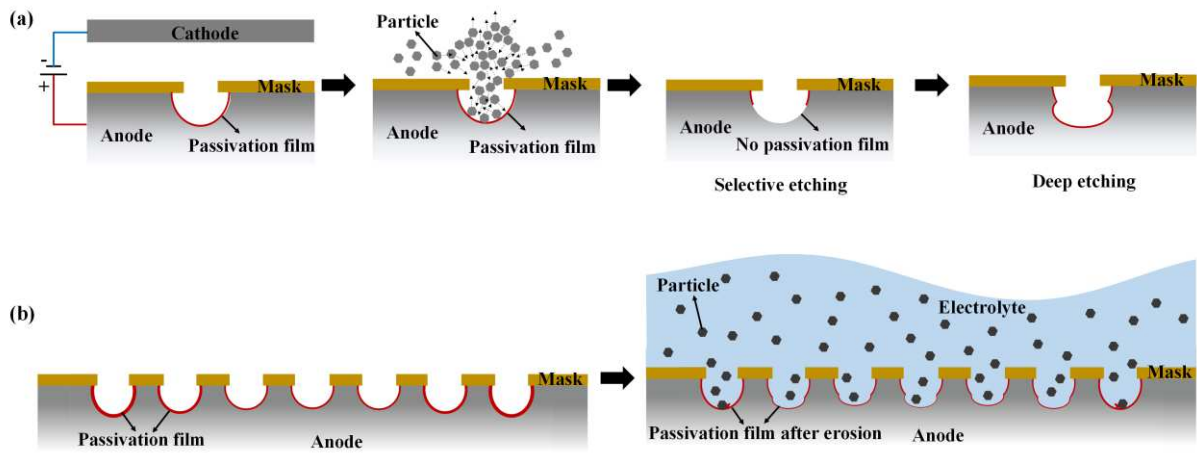


Fig. 1 Principle diagram of PA-TMEE: **a** effect of PA-TMEE on localization; **b** effect of PA-TMEE on uniformity

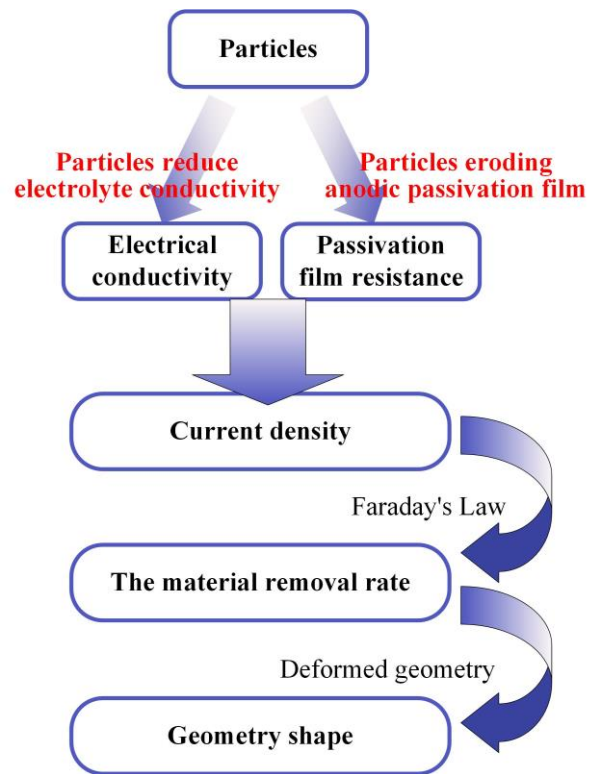


Fig. 2 Basic principle of the reaction model

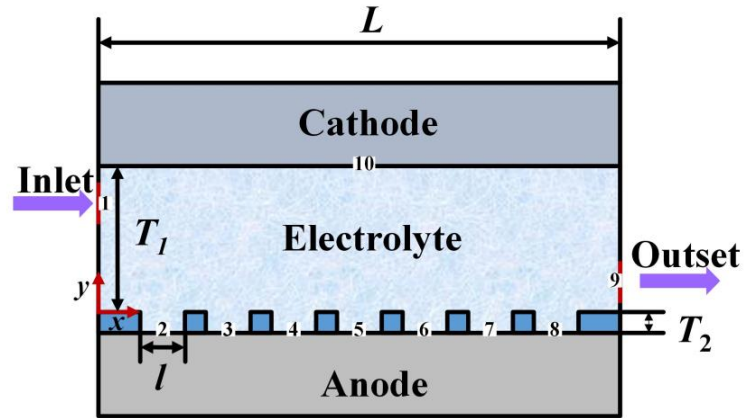


Fig. 3 PA-TMEE model for multi-physical field simulation

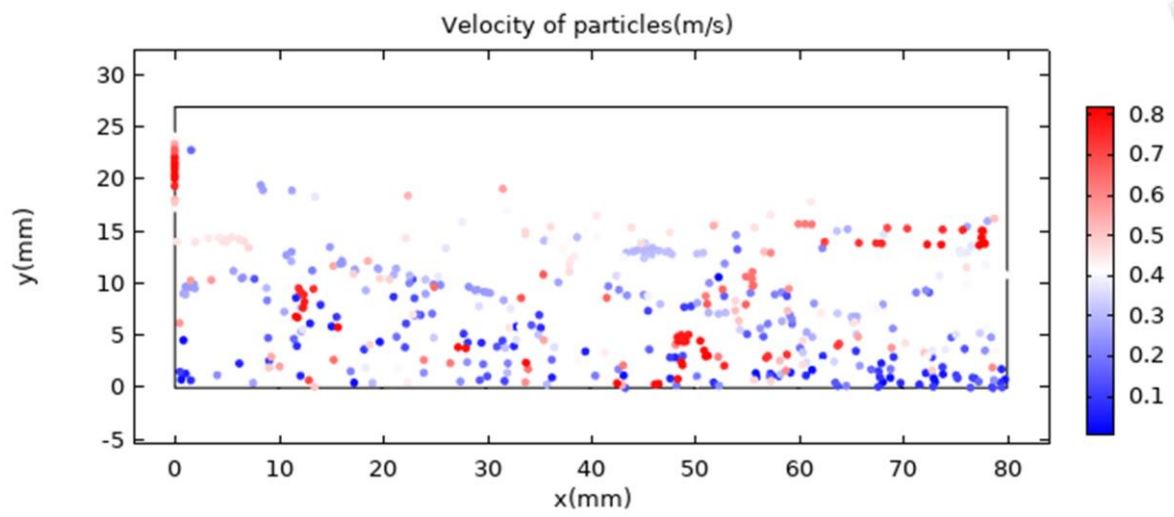


Fig. 4 The spatial distribution of SiC particles in the PA-TMEE

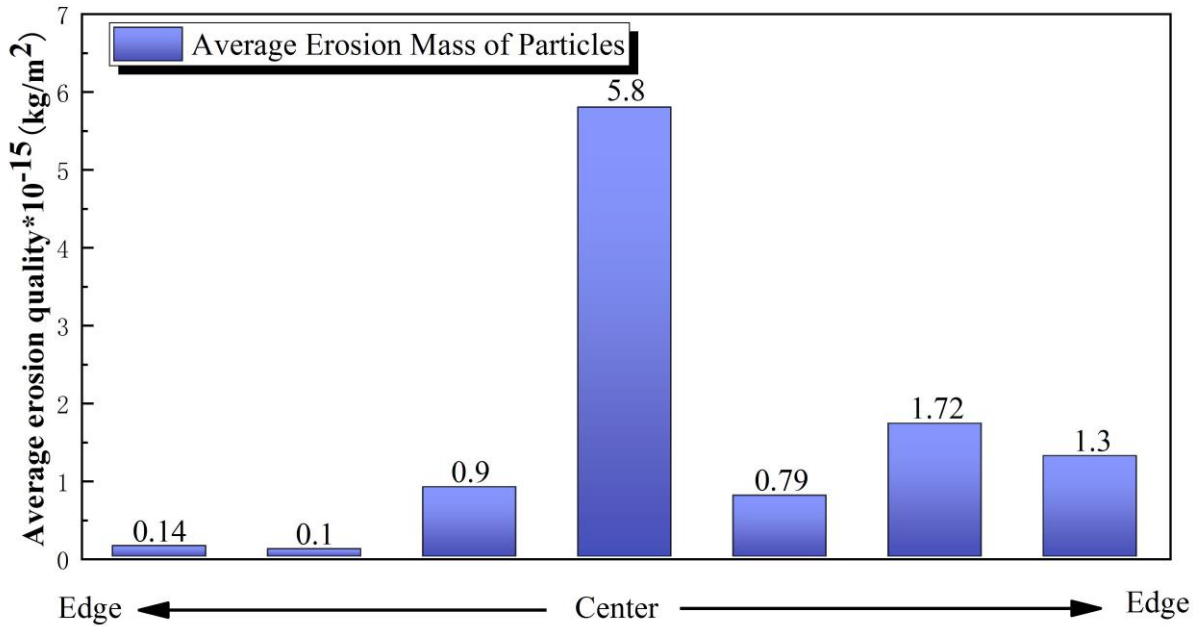


Fig. 5 Average erosion mass distribution of SiC particles on the surface of the micro pits

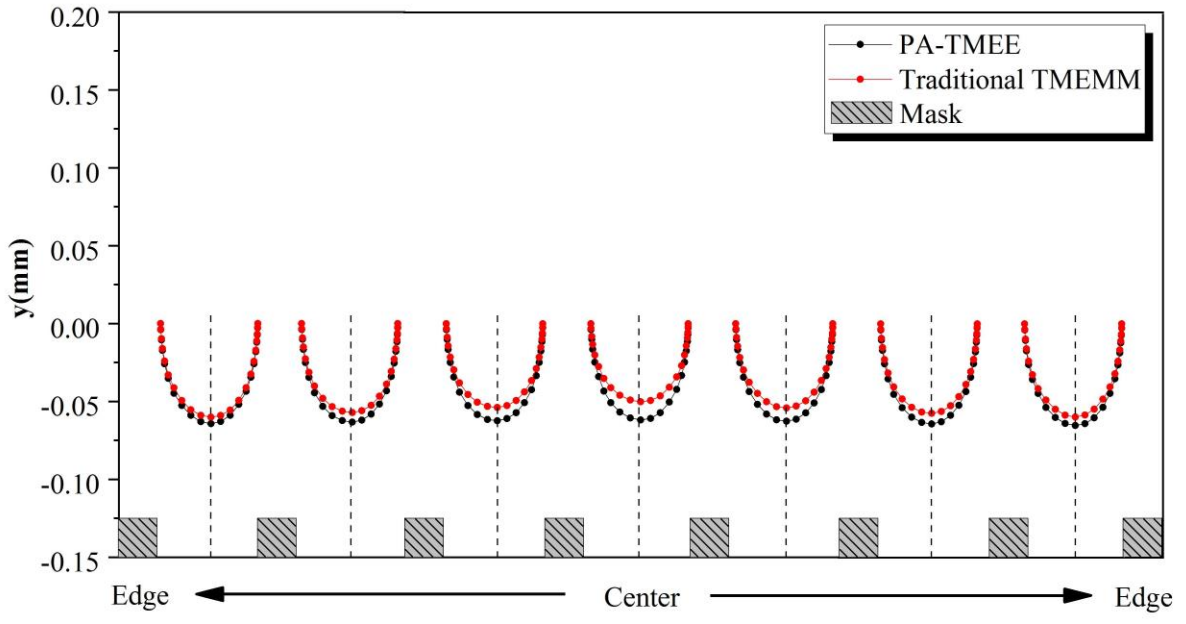


Fig. 6 Comparison of anode profiles with PA-TMEE and traditional TMEE

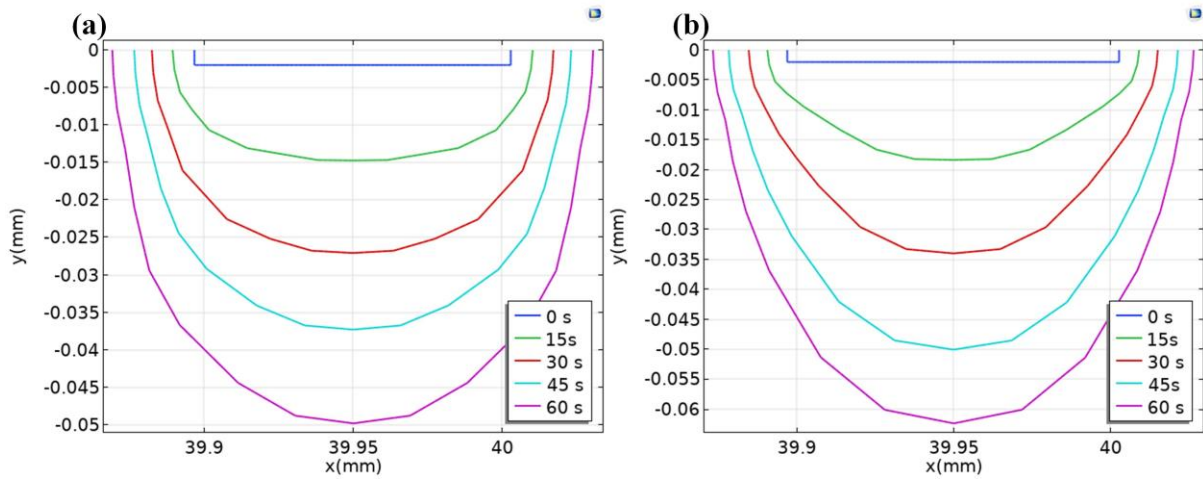


Fig. 7 Comparison of single micro pit profile with different machining methods. **a** traditional TMEE.

b PA-TMEE

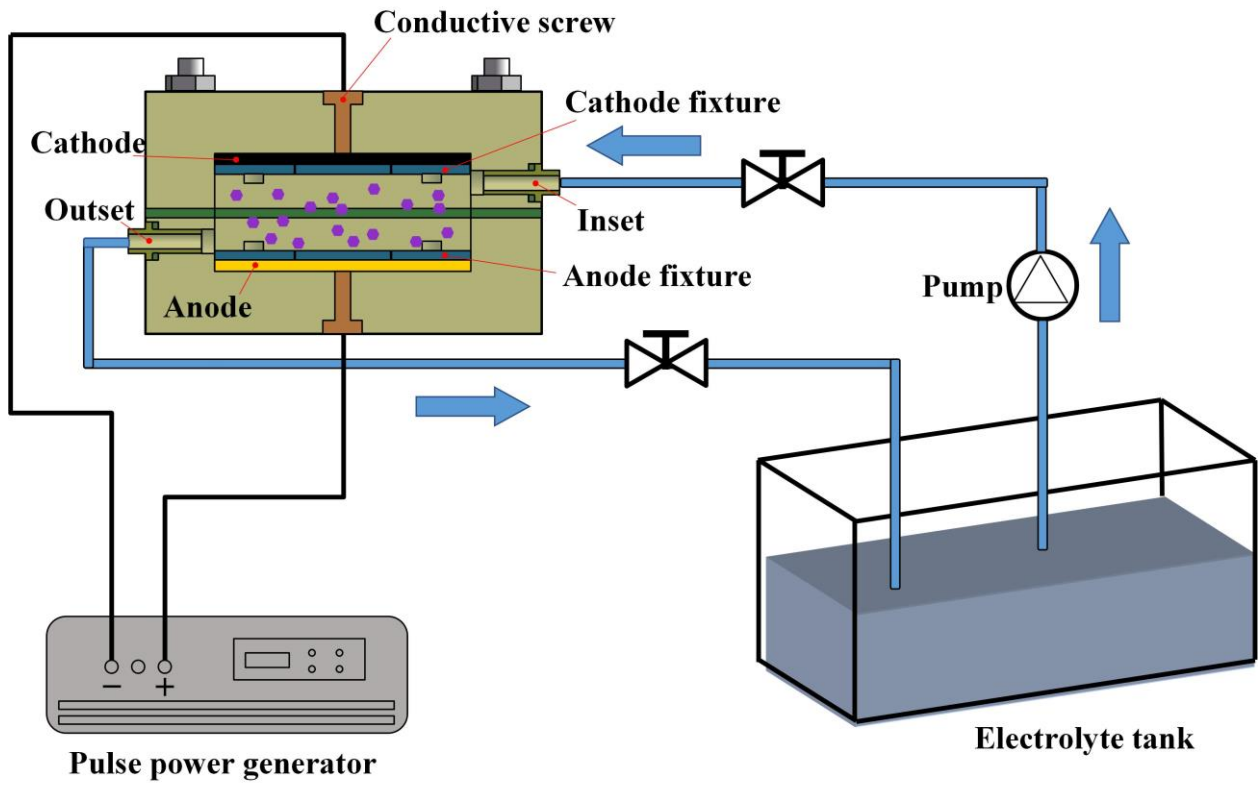


Fig. 8 The schematic view of PA-TMEE

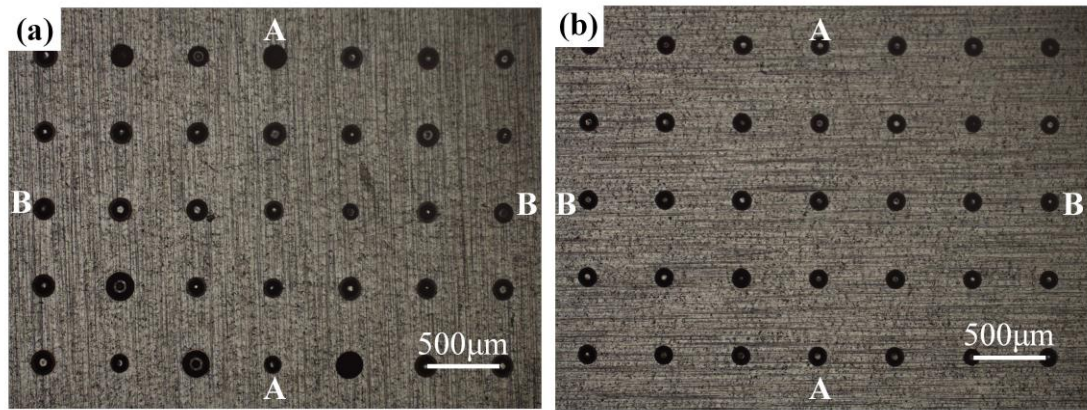


Fig. 9 Comparison of electrochemical etching results: **a** traditional TMEE; **b** PA-TMEE (A-A and B-B are the selected directions of the test points)

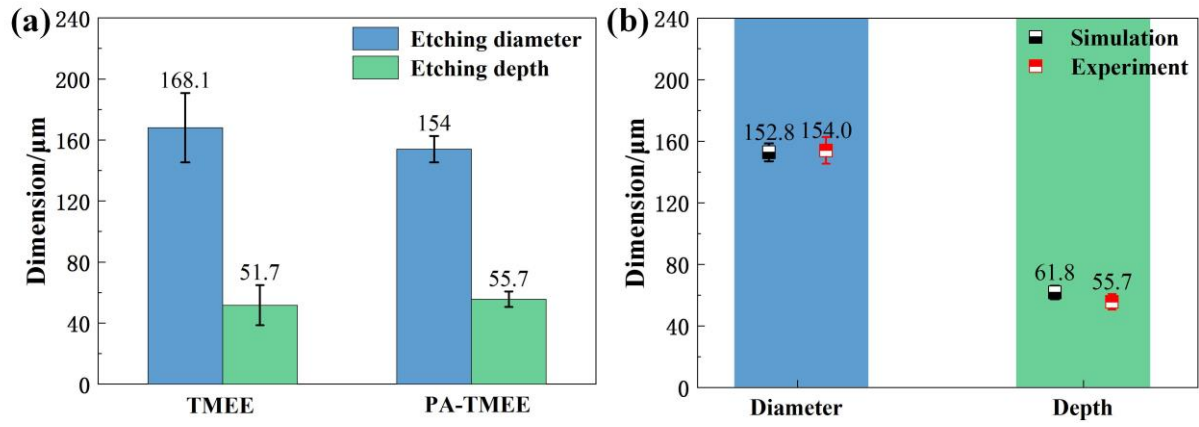


Fig. 10 Comparison of etching results: **a** comparison of etching diameter and etching depth for different machining methods; **b** comparison of simulated and experimental results of PA-TMEE

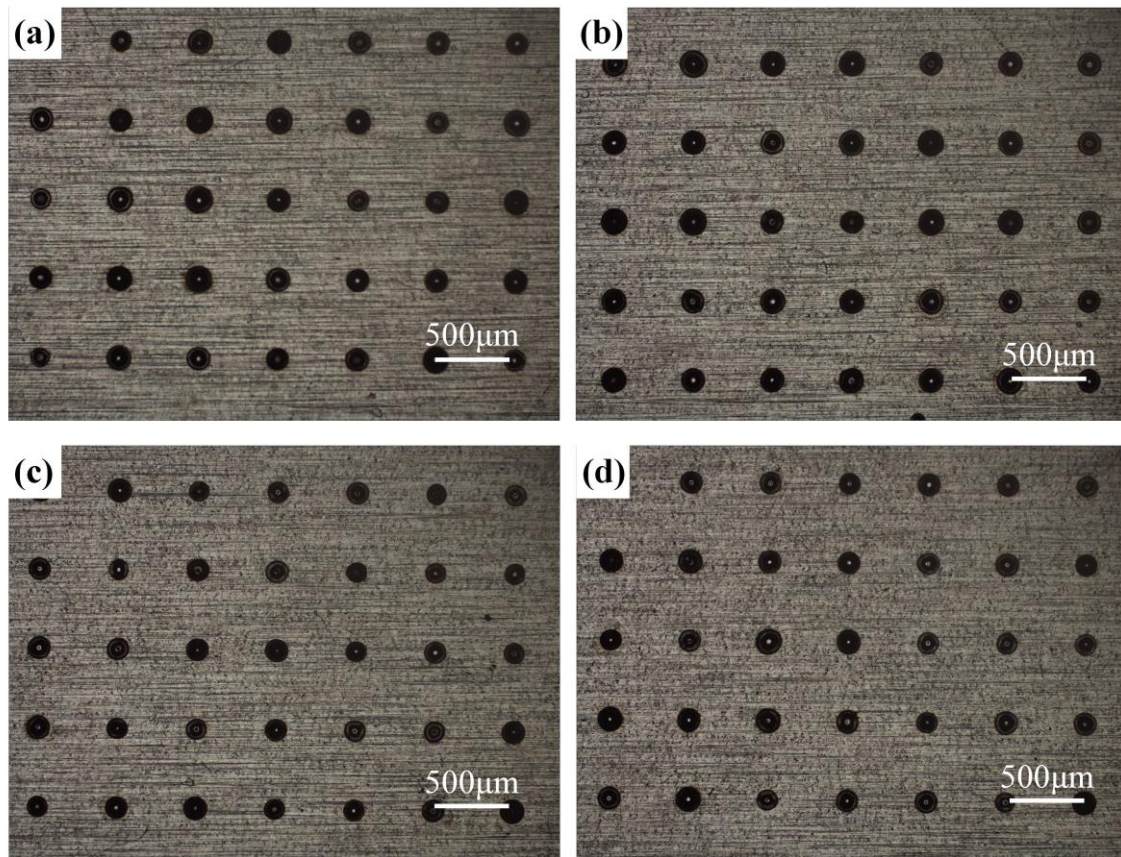


Fig. 11 Etching of micro pits with SiC particles of different diameters: **a** 10 μm ; **b** 20 μm ; **c** 40 μm ; **d** 60 μm

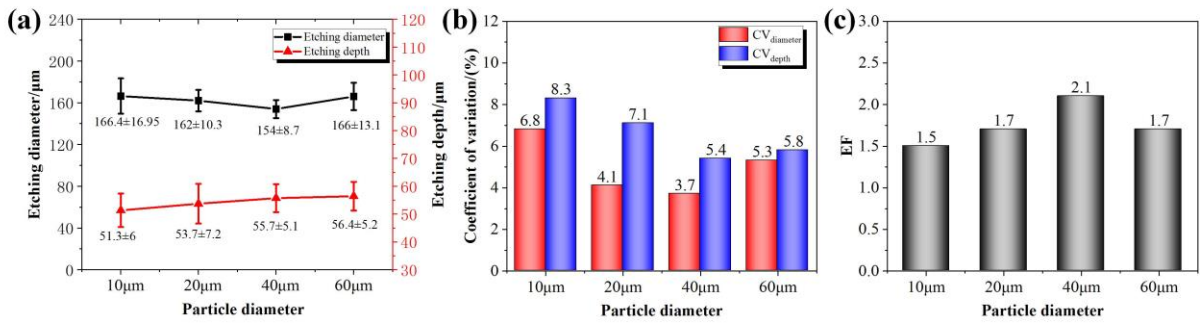


Fig. 12 Micro pits etched results with different particle diameters: **a** diameter and depth of micro pits; **b** CV value of micro pits diameter and depth; **c** EF of micro pits

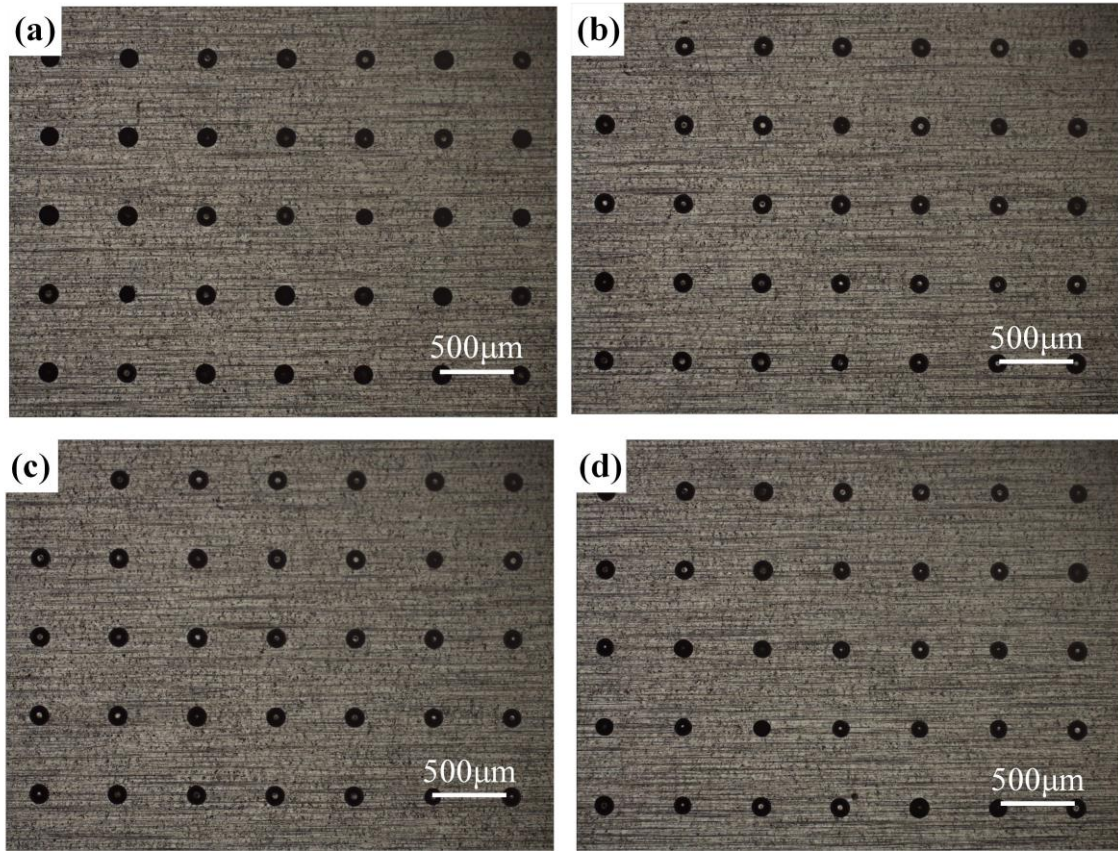


Fig. 13 Micro pits etching profiles at different 40 μm particle content: **a** 2 g/L; **b** 4 g/L; **c** 6 g/L; **d** 8 g/L

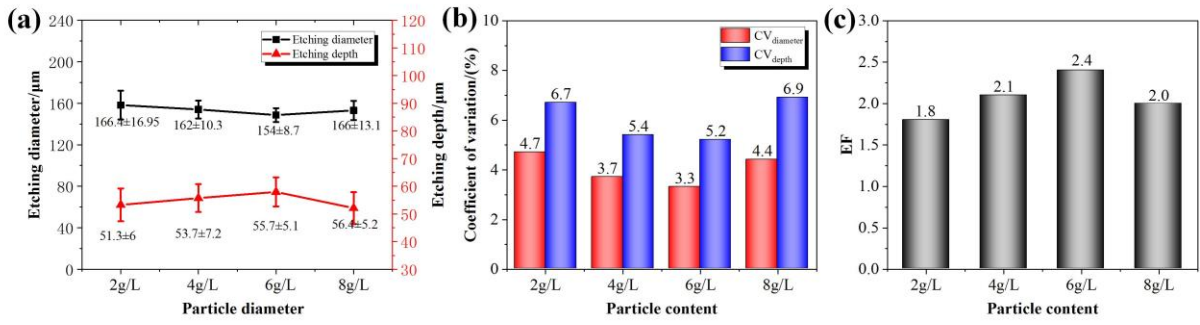


Fig. 14 Micro pits etching results with different particle content: **a** diameter and depth of micro pits; **b** CV value of micro pits diameter and depth; **c** EF of micro pits

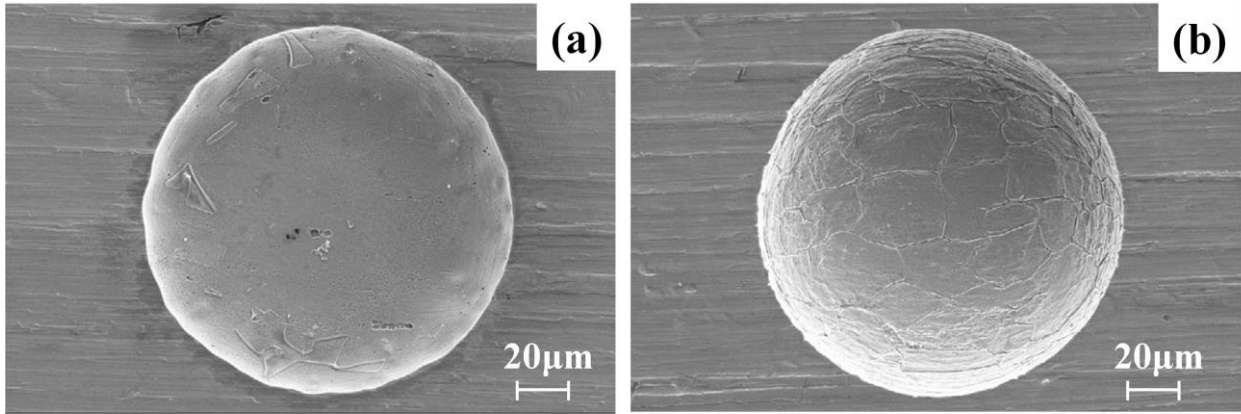


Fig. 15 Profiles of micro pits for different machining methods: **a** traditional TMEE; **b** PA-TMEE

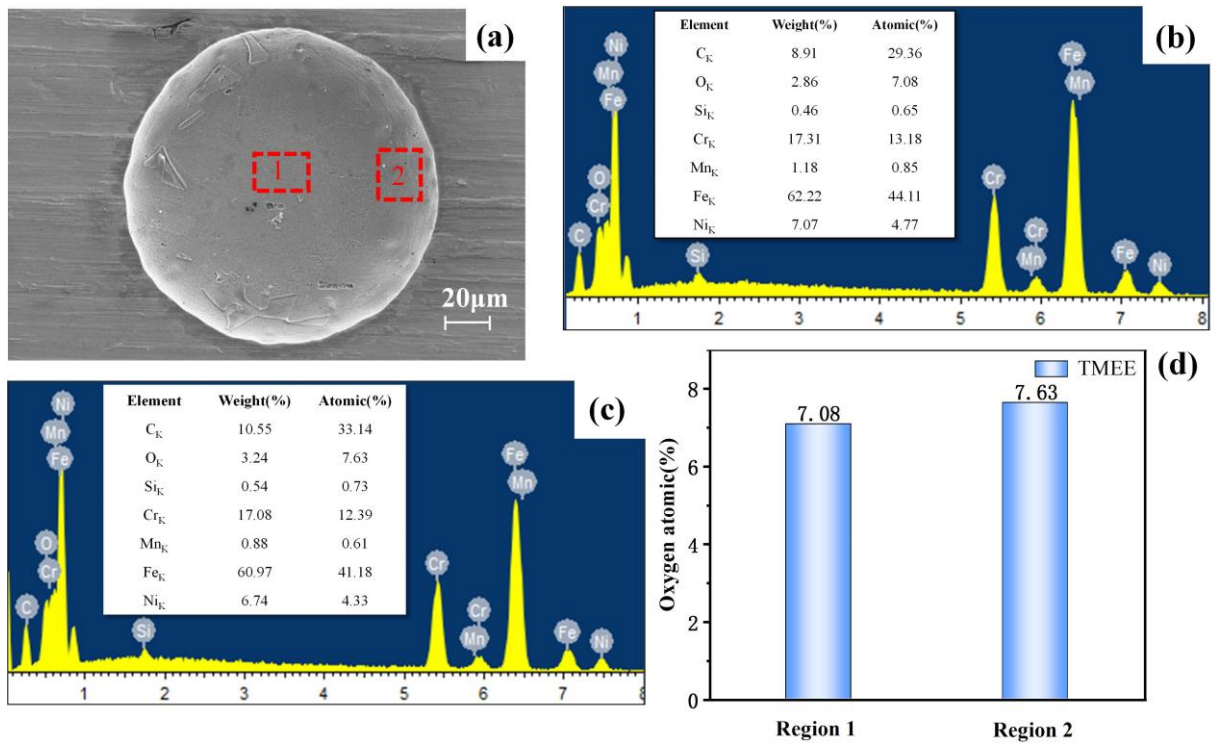


Fig. 16 **a** SEM image of the micro pit machined with TMEE; **b** EDS analysis of region 1; **c** EDS analysis of region 2; **d** comparison of the oxygen in regions 1 and 2

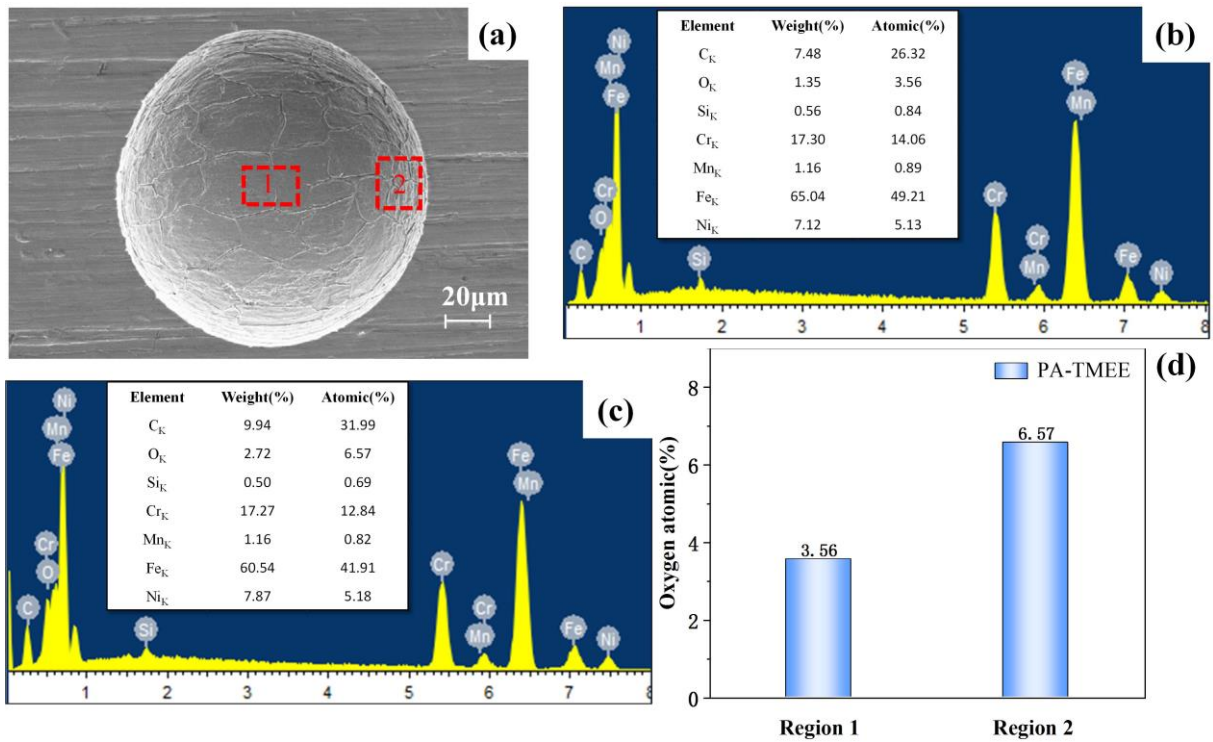


Fig. 17 **a** SEM image of the micro pit machined with PA-TMEE; **b** EDS analysis of region 1; **c** EDS analysis of region 2; **d** comparison of the oxygen in regions 1 and 2

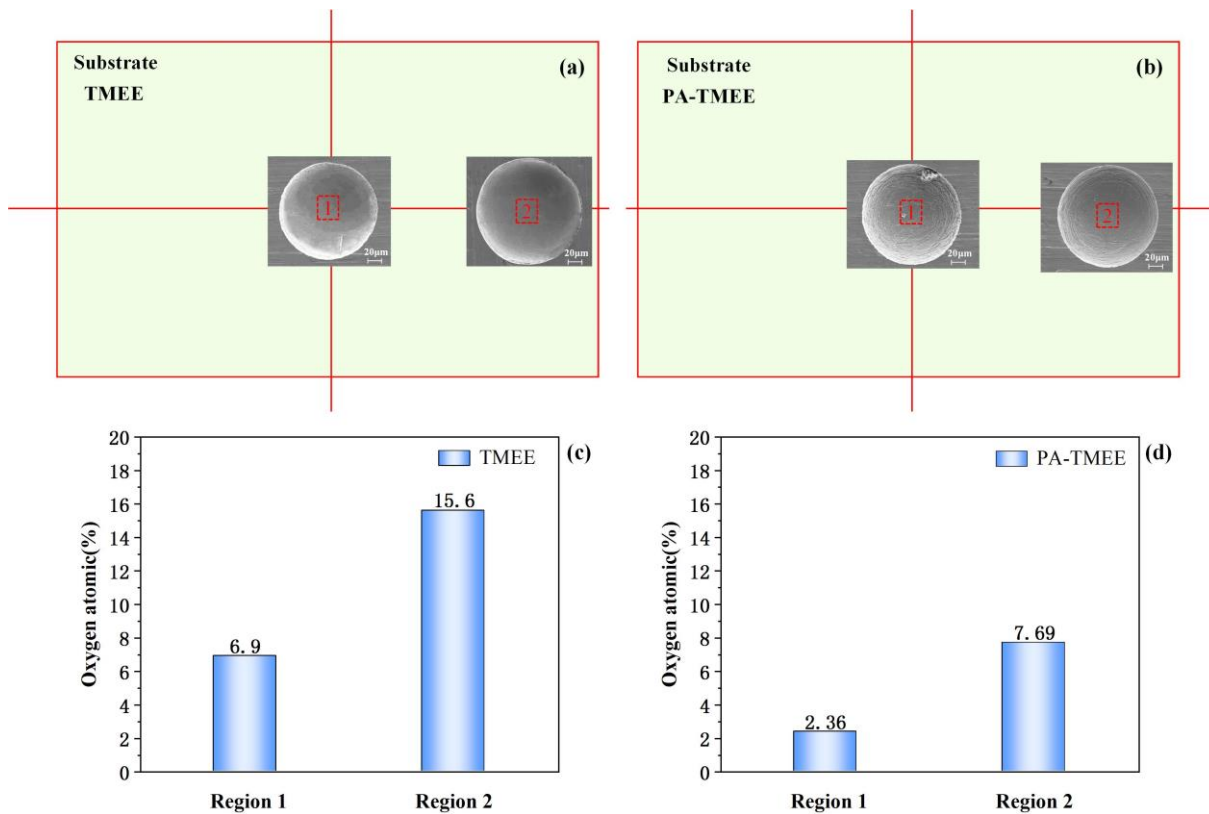


Fig. 18 **a** SEM image of the micro pits at the center and edge of the substrate obtained by TMEE; **b** SEM image of the micro pits at the center and edge of the substrate obtained by PA-TMEE; **c** the oxygen content of regions 1 and 2 in TMEE; **d** the oxygen content of regions 1 and 2 in PA-TMEE

Table 1 Parameters of the simulation

Simulation parameters	Value
Dynamic viscosity of the electrolyte, μ	$1.004 \times 10^{-3} \text{Pa} \cdot \text{s}$
Electrolyte density, ρ	1100kg/m^3
Electrolyte temperature, T	298K
Application Voltage, U	10V
Machining time, t	60s
Initial conductivity, κ_0	10S/m
Number of particles, n	3000

Table 2 Parameters of the etching experiments

Experiments	Experiment1	Experiment2
Comparison experiments	Traditional TMEE	PA-TMEE
Dispersion phase		SiC, 4 g/L, particle diameter 40 μm
Application voltage	10V	10V
Etching time	60s	60s
Flow rate	3L/min	3L/min
Electrolyte temperature	30°C	30°C

Table 3 The conductivity of electrolytes with different particle content

Particle content	2 g/L	4 g/L	6 g/L	8 g/L
Electrolyte conductivity	134.5 mS/cm	132.7 mS/cm	129.8 mS/cm	127.9 mS/cm